Available online at www.sciencedirect.com
SCIENCE DIRECT®
Journal of Solid State Chemistry 178 (2005) 120–127
JOURNAL OF SOLID STATE CHEMISTRY
www.elsevier.com/locate/jssc

Influence of dopant concentration on the structure and physical properties of $Nd_{1-x}Pb_xMnO_3$ single crystals

Nilotpal Ghosh[a], Suja Elizabeth[a], H.L. Bhat[a,*], G. Nalini[b], B. Muktha[b], T.N. Guru Row[b]

[a]*Department of Physics, Indian Institute of Science, Bangalore 560012, India*
[b]*Solid State and Structural Chemistry Unit, Indian Institute of Science, Bangalore 560012, India*

Received 6 April 2004; received in revised form 11 July 2004; accepted 14 July 2004

Abstract

The structure of $Nd_{1-x}Pb_xMnO_3$ crystal for $x = 0.25$ is determined at room temperature by single-crystal X-ray diffraction. The structural refinement reveals that the crystal is tetragonal with space group $P4/mmm$, $Z = 4$ and R of 8.3%. The lattice parameters are $a = 7.7652(1)$ Å, $c = 3.884(1)$ Å and $\alpha = \beta = \gamma = 90^\circ$. The structural analysis is then extended to $x = 0.38$. It is noticed that substitution of Pb at the Nd site results in structural phase change from tetragonal ($x = 0.25$) to cubic ($x = 0.38$). These changes are attributed to the progressive removal of inter-octahedral tilting and minimization of the octahedral distortion leading to a higher symmetry as doping concentration increases. While the unit cell volume of tetragonal structure ($P4/mmm$) is comparable to that of parent $NdMnO_3$ ($Pnma$), the volume of cubic unit cell ($Pm\bar{3}m$) is doubled. Electron diffraction patterns support these results and rule out the possibility of twinning. Changes in transport properties as a function of temperature at different doping levels are in accordance with the observed structural changes. It is observed that T_θ and T_{MI} increase with x.

Keywords: Manganites; Perovskite; Crystal structure; Superlattice; MI transition; Ferromagnetism; T_θ; T_{MI}

1. Introduction

Rare-earth manganites exhibiting colossal magnetoresistance (CMR) continue to attract research attention because of diverse physical properties and possible technological applications. Subtle structural changes between multiple phases and their relationship with physical properties have led to detailed structural investigations. The $RMnO_3$ perovskites (R is any rare earth between Lanthanum and Dysprosium) are orthorhombically distorted ($Pnma$) and isostructural with $GdFeO_3$ [1,2]. On the other hand, for rare-earths from Holmium to Lutetium as well as Yttrium, the crystal structure is hexagonal with space group $P6_3cm$ [2,3]. Substitution of trivalent lanthanides by divalent ions (Ca, Sr, Ba and Pb) leads to the simultaneous occurrence of Mn^{3+} and Mn^{4+} in the crystal lattice. This modifies the structural and physical properties significantly. A number of structural modifications have been discovered in manganite systems [4–7]. In general, majority of CMR compounds fall into two types: rhombohedral ($R\bar{3}m$) and orthorhombic ($Pnma/Pbnm$). A structural change is noticed in manganites with increase in divalent doping. For example, the structure of $La_{1-x}Sr_xMnO_3$ changes from orthorhombic ($Pnma$) to rhombohedral ($R\bar{3}m$) as doping concentration increases [6,8]. However, other symmetries are also observed as in the case of $Nd_{1-x}Sr_xMnO_3$ which changes from orthorhombic ($Imma$) to tetragonal ($I4/mcm$) system as x increases [9]. Symmetry relationships between perovskite polymorphs have been investigated from a group theoretical standpoint. This demonstrates a path of phase transitions through a sequence of space group–subgroup steps which is consistent with experiments [10].

The parent compounds ($LaMnO_3$, $NdMnO_3$ and $PrMnO_3$) are A-type antiferromagnetic insulators. Their insulating nature as well as anisotropic magnetic

*Corresponding author. Fax: +91-80-360-2602.
E-mail address: hlbhat@physics.iisc.ernet.in (H.L. Bhat).

0022-4596/$ - see front matter © 2004 Elsevier Inc. All rights reserved.
doi:10.1016/j.jssc.2004.07.016

interaction are related to structure. There are two characteristic distortions that influence the perovskite structure of manganites. One relates to co-operative tilting of MnO_6 octahedra which is established below 1000 K as a consequence of mismatch of ionic radii between the rare-earth and divalent ions [11]. This often takes the form of rigid rotation of the MnO_6 octahedra and modifies the co-ordination sphere of the *R*-site cation [12]. The other, Jahn–Teller (JT) distortion arises due to electronic instability of Mn^{3+} in the octahedral crystal field influencing the MnO_6 octahedra in such a way that there are long and short Mn–O bonds and deviations in O–Mn–O bond angles from 180°. These two distortions play a key role in structural evolution of perovskite manganites. Electronic transport is often strongly influenced by structural changes. For example, in $La_{1-x}Sr_xMnO_3$ the rhombohedral phase is metallic while the orthorhombic phase is insulating at low temperature [6,8] where as in $La_{1-x}Ca_xMnO_3$, the orthorhombic symmetry is retained both in insulating and metallic phases. Local structural features have profound influence on the conduction mechanisms in manganites [12]. As divalent ions are doped in these systems, the ferromagnetic (FM) double exchange (DE) Mn^{3+}–O–Mn^{4+} interaction begins to compete with antiferromagnetic (AFM) super exchange (SE) Mn^{3+}–O–Mn^{3+} interaction. It is to be noted that, the number of Mn^{4+} ions created because of divalent doping can be decreased as a result of oxygen off-stoichiometry [13]. In such a case, there can be only Mn^{2+} and Mn^{3+} ions. However, DE interaction will be still valid in presence of Mn^{2+} and Mn^{3+} ions. This has already been reported in the case of $La_{0.7}Ce_{0.3}MnO_3$ where tetravalent Ce^{4+} doping generates Mn^{2+} and Mn^{3+} [14]. The basic mechanisms of SE and DE interactions are mediated by the *d*-electron overlap between two transition metal ions via the intervening oxygen *p*-orbital. The extent of overlap depends on cation–oxygen–cation bond angle and cation–cation bond length in different perovskite systems [15–17]. In manganites, this overlap integral depends on Mn–O–Mn bond angle and Mn–Mn bond length which are sensitive to the tilt of neighboring MnO_6 octahedra [6,18]. Hence, it is interesting to study the influence of divalent dopant on the local structural modifications and the relevant physical properties. This paper reports the study of Pb substitution in $NdMnO_3$ and its impact on the structure, transport and magnetic properties.

2. Crystal growth

$Nd_{1-x}Pb_xMnO_3$ single crystals are obtained by high-temperature solution growth technique using PbO/PbF_2 solvent with Nd_2O_3, $MnCO_3$ and PbO in stoichiometric quantities as solute [19]. The homogenized mixture was contained in a platinum crucible and growth was carried out in a resistive furnace. The cationic ratio was varied to obtain a range of x values. The composition of resulting crystals was determined by Energy Dispersive X-ray (EDX) Analysis followed by Inductively Coupled Plasma Emission Spectroscopy (ICPAES) for better accuracy.

3. Structural studies

A crystal of nominal lead content $x = 0.25$ and size $0.3 \times 0.2 \times 0.04\,mm^3$ was mounted on a BRUKER AXS SMART APEX CCD diffractometer [20] at a distance of 6.03 cm from the detector. The diffraction intensities were measured with monochromated Mo$K\alpha$ radiation ($\lambda = 0.7107$ Å). The orientation matrix was obtained at room temperature from reflections derived from 50 frames to give the tetragonal unit cell (Table 1). Data were collected in four batches covering a complete sphere of reciprocal space with each batch at different ϕ angles ($\phi = 0°, 90°, 180°, 270°$) and each frame covering 0.3 degree in ω at 10 s exposure time. The data were 98.7% complete to 56° in 2θ. An approximate empirical absorption correction was applied assuming the crystal shape to be cylindrical. Positional co-ordinates of Nd and Mn atoms were obtained by direct methods in the space group $P4/mmm$ using the SHELXS97 module and refined by SHELXL97 [21]. The Nd atoms occupy three crystallographically distinct sites (2*e*, 1*d* and 1*b*). In order to account for the presence of Pb in any of Nd sites, occupancy refinements were carried out (constraining the overall site occupancy to 1.0) indicating that the Pb atom fully occupies the 1*d* site and amounts to the presence of 25% of Pb at Nd sites. Hence, refinement confirms that Pb and Nd occupy different crystallographic sites (1*d* and 2*e*, 1*b*, respectively). Difference Fourier synthesis revealed the positions of the remaining oxygen atoms, which were included in the refinement. The occupancy refinements on the oxygen atoms suggest an occupancy of 96% for O(1) and 80% for O(3) leading to an acceptable *R* index of 8.3% (Table 2). This oxygen off-stoichiometry and the composition are consistent with the results of compositional analysis by ICPAES. The residual density is quite high (Table 1) because of presence of heavier atoms which is usual for inorganic compounds. The results of measurement and structural refinement are summarized in Table 1. The atomic coordinates along with the equivalent thermal parameters are listed in Table 2. The packing diagram of tetragonal lattice is shown in Fig. 1. The selected bond lengths and bond angles for $x = 0.25$ are shown in Table 3. The neutron diffraction studies of the crystal with nominal composition $Nd_{0.7}Pb_{0.3}MnO_3$ (carried out to analyze the magnetic structure, details of which will be reported elsewhere) revealed that the

Table 1
Crystal data, measurements and refinement parameters for $Nd_{0.75}Pb_{0.25}MnO_{2.72}$

Crystal data	
Empirical formula	$Nd_{0.75}Pb_{0.25}MnO_{2.72}$
Crystal symmetry	Tetragonal
Crystal habit, color	Blocks, black
Crystal size (mm)	$0.3 \times 0.2 \times 0.04\,mm^3$
Crystal system	Tetragonal
Space group	$P4/mmm$
Cell dimensions (Å)	$a = 7.7652(1),\ c = 3.884(1)$
Volume (Å^3)	234.19(7)
Formula weight	258.23
Density (calculated)	$6.35\,g/cm^3$
Z	4
$F(000)$	457.8
Data collection	
Equipment	Bruker APEX SMART CCD
λ(Mo$K\alpha$ (graphite monochromator)) (Å)	0.7107
Scan mode	ω scan
Temperature (K)	298
θ range (deg)	2.8–28
Recording reciprocal space	$-10 \leqslant h \leqslant 9$ $-10 \leqslant k \leqslant 9$ $-5 \leqslant l \leqslant 5$
Number of measured reflections	1336
Number of independent reflections	202[$R_{int} = 0.0443$]
μ (mm^{-1})	39.471
Refinement	
Number of refined parameters	18
Refinement method	Full matrix least squares
$R[I > 4\sigma I]/R$[all data]	0.083/0.087
w$R[I > 4\sigma I]/R$[all data]	0.233/0.226
GoF	1.323
Max/min $\Delta\rho$(Å e^{-3})	3.987/−3.448

Table 2
Final atomic coordinates and equivalent thermal parameters (U_{equvi}) at 298 K for $Nd_{0.75}Pb_{0.25}MnO_{2.72}$

Atom	x	y	z	Site	Occupancy	U_{equvi}
Nd1	1/2	0	1/2	2*e*	1.0	0.0322(12)
Pb1	1/2	1/2	1/2	1*d*	1.0	0.02444(10)
Nd2	0	0	1/2	1*b*	1.0	0.0730(26)
Mn1	0.2504(4)	0.7496(4)	0	4*j*	1.0	0.0261(16)
O1	0.2562(6)	0.7438(6)	1/2	4*k*	0.96(4)	0.0926(241)
O2	0	0.7492(7)	0	4*l*	1.0	0.1002(215)
O3	0.2655(9)	1/2	0.0	4*n*	0.80(3)	0.1009(268)

The equivalent thermal parameter is defined as $U_{equvi} = -(2\pi^2 (U_{11}(ha^*))^2 + (U_{22}(kb^*))^2 + (U_{33}(lc^*))^2 + 2U_{12}hka^*b^* + 2U_{12}hla^*c^* + 2U_{23}klb^*c^*)$.

structure of this crystal is also the same as that for $x = 0.25$ and $a = 7.78$ Å, $c = 3.48$ Å with space group $P4/mmm$.

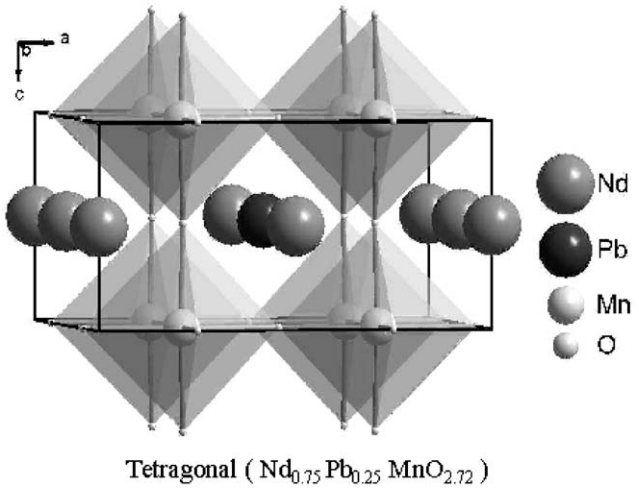

Fig. 1. Packing diagram of $Nd_{0.75}Pb_{0.25}MnO_{2.72}$ along the *b*-direction.

Table 3
Selected geometric parameters (bond lengths (Å) and bond angles (deg)) for $Nd_{0.75}Pb_{0.25}MnO_{2.72}$

2 × Mn1–O1 = 1.943(1)	O1–Mn1–O1 = 176(3)
2 × Mn1–O1 = 1.943(1)	O3–Mn1–O2 = 176(3)
2 × Mn1–O2 = 1.944(4)	Mn1–O1–Mn1 = 176(2)
2 × Mn1–O2 = 1.944(4)	Mn1–O2–Mn1 = 179(3)
2 × Mn1–O3 = 1.942(7)	Mn1–O3–Mn1 = 173(4)
4×(Ndl–O1) = 2.74(3)	Mn1–O3–Mn1 = 173(4)
4×(Ndl–O2) = 2.749(1)	Mn1–O3–Mn1 = 173(4)
4×(Ndl–O3) = 2.832(1)	Mn1–O3–Mn1 = 173(4)
4×(Nd2–O1) = 2.81(3)	Mn1–O3–Mn1 = 173(4)
4×(Nd2–O2) = 2.75(3)	Mn1–O3–Mn1 = 173(4)
4×(Pbl–Ol) = 2.67(3)	Mn1–O3–Mn1 = 173(4)
4×(Pbl–O3) = 2.66(4)	Mn1–O3–Mn1 = 173(4)

To extend our structural study, we have carried out single-crystal diffraction experiment for $Nd_{1-x}Pb_xMnO_3$ at higher Pb ($x = 0.38$) in the similar way. This crystal could be uniquely indexed into the cubic system of $a = 7.737$ (2) Å, volume = 463.22 (2) Å^3 and $Z = 8$. The structural solution could be obtained in $Pm\bar{3}m$ space group. However, the data could not be refined to an acceptable R index which may be attributed to the poor quality data and also excessive absorption due to high Pb content. Consequently, the empirical absorption correction did not work well. The evaluated Mn–O–Mn bond angles are approximately 178° and Mn–O bond lengths are almost equal (around 1.93 Å). It is to be noted that, the present system with $x = 0.38$ could not be indexed to any other crystal system except cubic. Moreover, even in the cubic system, the figure of merit (FOM) of the solution is the least for space group $Pm\bar{3}m$. The data could be refined to an R factor of 16%. Further refinements did not improve the thermal parameters and hence the high R factor. Since the co-ordinates obtained for all the atoms indicate

Table 4
Final atomic coordinates at 298K for $Nd_{0.62}Pb_{0.38}MnO_{2.7}$

Atom	x	y	z	Site
Nd1	0	0	0	1*a*
Nd2	0	1/2	1/2	3*c*
Nd3	1/2	1/2	1/2	1*b*
Pb1	0	1/2	0	3*d*
Mn1	0.2499(4)	0.2499(4)	0.2499(4)	8*g*
O1	0.2460(40)	0.2460(40)	1/2	8*g*
O2	0.2520(30)	0.2520(30)	0	12*i*

special positions, we have calculated bond distances using these values. The co-ordinates of atoms for cubic structure are given in Table 4.

In order to rule out the possibility of twinning in grown crystals, electron diffraction experiments are carried out. The single crystals are crushed and broken into tiny pieces. They are then mounted in a copper ring and the diffraction pattern is taken in transmission mode. Electron diffraction patterns given in Figs. 2(a) and (b) show no evidence of twinning for both the crystals with $x = 0.25$ and 0.38. There is no evidence of streak present in the electron diffractograms which shows that the quality of crystals is good. We will elaborate the significance of electron diffraction study in the section of "Results and Discussions".

4. Physical properties

Transport and magnetization measurements were carried out on crystals of various doping levels. Resistivity was measured by usual four probe technique, making four linear contacts on the sample by Ag–In alloy in the temperature range 300–80 K and shown in Fig. 3. Magnetic properties were determined by AC susceptibility measurements at 100 Hz and 5 Oe in the temperature range 78–240 K. All the doped crystals exhibited a paramagnetic to ferromagnetic transition as the temperature is lowered (Fig. 4). When the inverse susceptibility is plotted against temperature, the Curie–Weiss temperature T_θ is seen to progressively shift towards higher temperature as x value increases. A typical inverse susceptibility plot is shown in the inset of Fig. 4 for $x = 0.3$.

5. Results and discussions

The electron diffraction patterns obtained for doped crystals reveal some interesting features. In them, we have found superlattice spots in two directions for a crystal with $x = 0.25$ and in three directions for $x = 0.38$. These results reflect the fact that, $Nd_{1-x}Pb_xMnO_3$

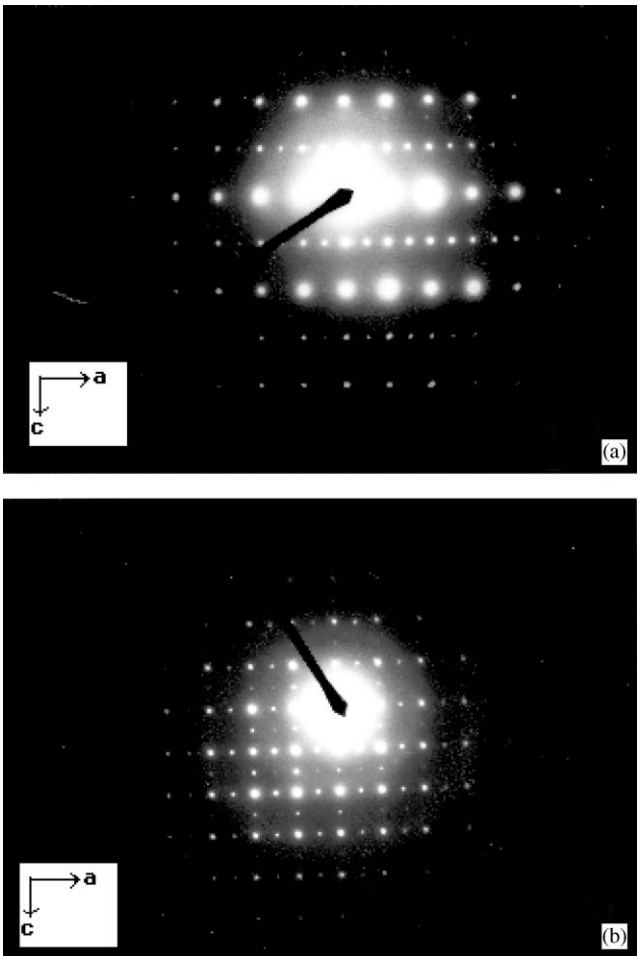

Fig. 2. Electron diffraction patterns of $Nd_{1-x}Pb_xMnO_3$ for (a) $x = 0.25$ and (b) $x = 0.38$, respectively.

goes to tetragonal to cubic phase as x is increased. Superlattice spots are seen along a direction for tetragonal ($x = 0.25$) and along a and c directions for cubic crystal ($x = 0.38$). Since, $a = b$ for tetragonal structure, the doubling of lattice parameters occurs in these two directions. Consequently in the electron diffraction pattern shown in Fig. 2(a) superlattice spots are seen only along a. On the other hand, for cubic unit cell, the lattice parameter doubling has occurred in all three directions since $a = b = c$. Hence, in the electron diffraction pattern taken for the cubic phase, the super lattice spots are seen both along a and c (Fig. 2(b)). The parent $NdMnO_3$ has an inherent perovskite distortion due to the presence of Nd in the R-site. As Nd is partially replaced by the larger cation Pb, the distortion is progressively reduced and the symmetry becomes tetragonal at 25% substitution. The distortion is almost removed in the case of 38% lead substitution which results in cubic symmetry as well as cell doubling. This is also evident from the electron diffraction pattern (Fig. 2(b)). The unit cell parameters can be related as $a_t = b_t \approx 2a_p$; $c_t \approx a_p$ for tetragonal structure and

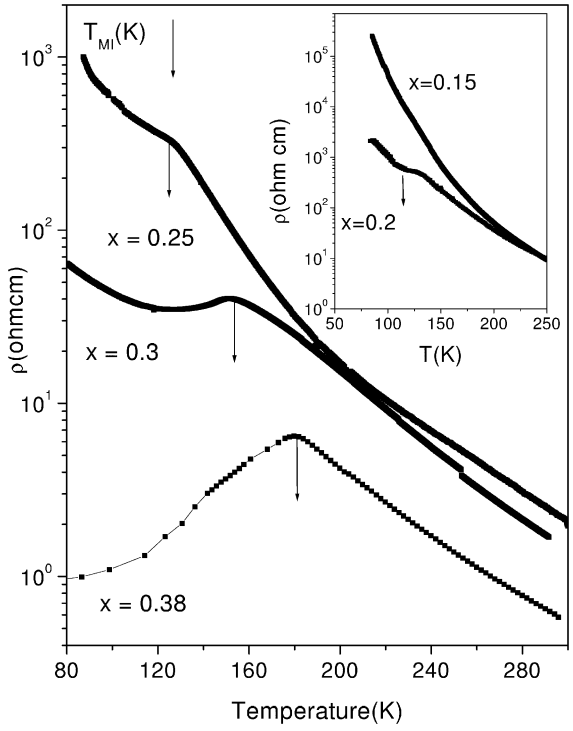

Fig. 3. Resistivity vs. temperature plots of $Nd_{1-x}Pb_xMnO_3$ for $x = 0.25$, 0.3 and 0.38 in the range of 80–300 K. The inset shows the resistivity profiles for $x = 0.15$ and 0.2 as a function of temperature.

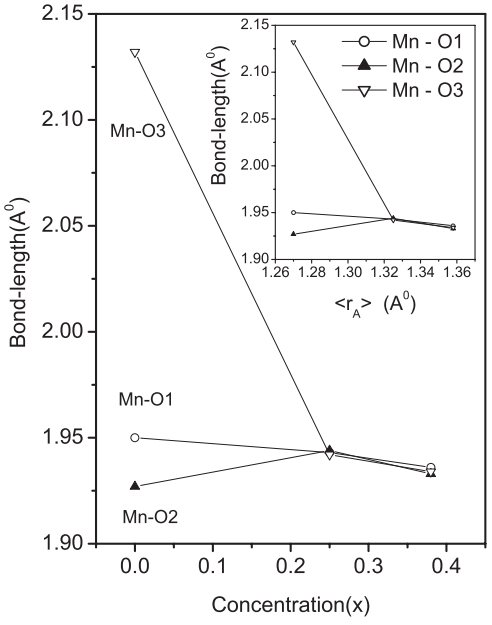

Fig. 4. The AC susceptibility plots for $x = 0.25$, 0.3 and 0.38 at 100 Hz and magnetic field $\sim$ 5 Oe. The inset shows inverse susceptibility vs. temperature plot for $x = 0.3$.

$a_c \approx 2a_p$ for cubic structure where a_p is cell parameter of ideal primitive ($Pm\bar{3}m$) perovskite structure. This is consistent with our crystal structure data. The unit cell consists of corner sharing MnO_6 octahedra in which Mn–O bonds become nearly equal as the structure changes from tetragonal to cubic. All Mn–O–Mn bond angles are also nearly same (178°(3)) in cubic structure while they are dissimilar in the tetragonal phase. Consequently the co-operative tilting of MnO_6 octahedra observed in $NdMnO_3$ is reduced considerably in $Nd_{0.75}Pb_{0.25}MnO_{2.72}$ and is the least in $Nd_{0.62}Pb_{0.38}MnO_{2.7}$. It is to be pointed out that the oxygen deficiency is known to occur in manganites [13]. Aleksandrov [22] and Barnighausen [23] investigated the existence of symmetry relationship between perovskite polymorphs from the view point of group theory. Aleksandrov reports transition routes from $Pm\bar{3}m$ to *Pnma* symmetry via five intermediate space groups [10]. On the other hand, Barnighausen demonstrated path of continuous phase transitions from $Pm\bar{3}m$ to *Pnma* symmetry via a sequence of space group–subgroup steps $Pm\bar{3}m$–$P4/mmm$–*Cmmm*–*Icmm*–*Pbnm*(*Pnma*) [10]. The structural transformation route observed in the present investigation is in accordance with Barnighausen's prediction, although intermediate stages like *Cmmm* and *Icmm* were not observed. These intermediate structures might be discernible at other doping concentrations.

Fig. 5 shows the variation of different Mn–O bond lengths with divalent dopant concentration. The static distortion of MnO_6 octahedra is maximum for parent orthorhombic $NdMnO_3(x = 0)$ [24]. The mismatch between different Mn–O bond lengths of $Nd_{1-x}Pb_xMnO_3$ is much less at $x = 0.25$ and 0.38. In manganites, $\langle r_A \rangle$ gives the measure of one electron (e_g) band width [12] which is very sensitive to the concentration and ionic radii of divalent dopant. It is noted that when $\langle r_A \rangle = 1.325$ Å ($x = 0.25$) the Mn–O bond lengths are almost equal (inset of Fig. 5). The distortion in perovskite unit cell consequent to its octahedral tilting is estimated by the tolerance factor (t_G). The structural change of $Nd_{1-x}Pb_xMnO_3$ from orthorhombic to cubic (via tetragonal) with increase in x is consistent with the t_G approaching unity. The dependence of t_G on dopant concentration (x) is shown in Fig. 6.

It is seen from the temperature dependence of resistivity (Fig. 3) that the metal–insulator transition temperature (T_{MI}) (vertical arrows in the figure) increases with x. The magnitude of resistivity at room temperature decreases with increase of x. This is attributed to the increment of Mn–O–Mn bond angle with x (or $\langle r_A \rangle$) which results in increase of Mn–Mn electron hopping rate [25]. The plot for sample with $x = 0.25$ has a small hump at around 127 K suggesting the onset of MI transition. However, the sample exhibits an insulating behavior as temperature is further lowered. The resistivity profile for a sample with $x = 0.3$ has more prominent signature of metal to insulator transition (MI) at around 146 K, although as temperature

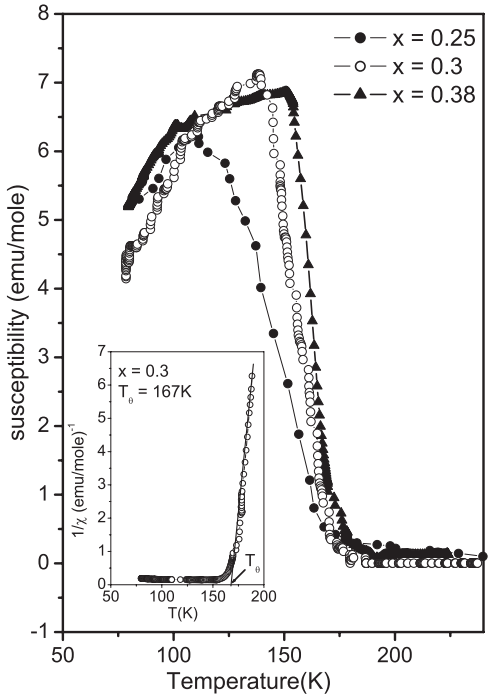

Fig. 5. Mn–O bond lengths as a function of lead concentration. Inset: Mn–O bond lengths as a function of $\langle r_A \rangle$. The points indicate experimental data and the lines are guide to the eye. The data for $x = 0$ has been taken from Ref. [24].

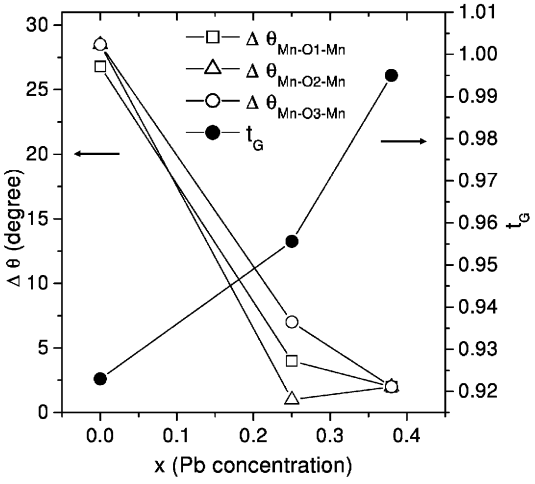

Fig. 6. Tolerance factor (t_G) and $\Delta\theta$ plotted as a function of Pb concentrations (x), where $\Delta\theta = 180 - \theta_{\mathrm{Mn-O-Mn}}$. The points indicate experimental values and line guide to the eye. The data for $x = 0$ has been taken from Ref. [24].

decreases the profile takes the up turn showing insulating nature. The clear metallic phase at low temperature is seen for $x = 0.38$. As a matter of fact, the resistivity profiles of $Nd_{1-x}Pb_xMnO_3$ for different x values show that, the MI transition sets in at $x = 0.2$ and becomes gradually more prominent as x increases. This is evident from the inset of Fig. 3, which shows that sample with $x = 0.15$ is insulating down to low temperature. Furthermore, $x = 0.2$ sample has a slope change around 127 K and MI transition seems to set in at this concentration. Thus, it can be inferred that metal–insulator transition occurs when $\langle r_A \rangle$ exceeds a critical value $r_{\mathrm{MI}} = 1.314$ Å at $x = 0.2$. Since, samples with $x = 0.25$ and 0.38 have $\langle r_A \rangle$ more than 1.314 Å, the occurrence of MI transition for them is natural. Moreover, the Mn–O bond lengths are almost equal at $\langle r_A \rangle = 1.325$ Å for the sample with $x = 0.25$ (Fig. 5). This can be due to the removal of static coherent distortion of MnO_6 octahedra which causes charge localization in the metallic phase [26]. Similarly, the existence of low temperature metallic phase for $Nd_{1-x}Pb_xMnO_3$ at $x = 0.38$ can also be attributed to its less distorted cubic structure.

The direct exchange interaction between Mn ions is not possible in manganites because of the intervening oxygen. According to Goodenough [27], the nature of interaction depends on the extent of overlap between Mn d-orbitals and O p-orbitals which is very sensitive to Mn–Mn distance. In the Mn–O–Mn bonding patterns, if both Mn–O bonds are covalent the Mn–Mn distance will be the shortest and interaction will be antiferromagnetic (AFM). If one Mn–O bond is covalent and the other is ionic, the Mn–Mn separation is larger and results in ferromagnetic (FM) interaction. Magnetic properties of $NdMnO_3$ where in-plane FM and out-of-plane AFM interactions have been noticed [12,27] are consistent with this theoretical prediction. However, the predominant mechanism involved in doped $NdMnO_3$ is Double Exchange (DE) ferromagnetic interaction. AC susceptibility data shown in Fig. 4 clearly exhibit the presence of FM phase at low temperature in the range of x of the present investigation. The down turn in AC susceptibility profiles below 100 K can be attributed to a special ordering of Nd and Mn sublattices, which is already discussed else where [19].

In doped systems, Mn^{4+}–O–Mn^{3+} bonding arrangement is degenerate with Mn^{3+}–O–Mn^{4+}. This implies charge hopping between Mn ions leading to metallicity which is the key mechanism of DE interaction. However, it is to be noted that, the present samples are highly oxygen off-stoichiometric. Since oxygen content is around 2.72, the average oxidation state of Mn ions will be around 2.69 (for $x = 0.25$ sample). In this situation, probably no Mn^{4+} ion will exist in the crystal; rather there will be only Mn^{2+} and Mn^{3+} ions. Nevertheless, DE interaction will be still valid here as already mentioned before [14]. As a result, metallic phase is observed clearly in the present case at $x > 0.3$ (Fig. 3). In DE, Mn–Mn distance is shorter than that of the other ferromagnetic case (described before) and hopping integral between Mn d-orbitals is proportional to $\cos(\theta_{ij}/2)$ where θ_{ij} is the angle between two Mn moments at i and j sites [28]. Since, the direction of the Mn moment relative to the axes of the MnO_6

octahedron is determined in large part by crystal field, it is expected that θ_{ij} will depend on the Mn–O–Mn tilt angle [6]. Therefore, the hopping rate will depend on Mn–O–Mn bond angle ($\theta_{Mn-O-Mn}$) [6,18,25] which in turn will depend on the magnitude of tilt between two neighboring octahedra. The deviation of Mn–O–Mn bond angle from 180° ($\Delta\theta = 180 - \theta_{Mn-O-Mn}$) is maximum in $NdMnO_3$ and decreases with increase of x (Fig. 6). The Mn–Mn bond distances and corresponding magnetic interactions for various dopant concentration are shown in Table 5. These bond distances have been calculated from the present structural solutions. Thus, it is evident that structural changes due to doping play an important role to control the physical properties of the system.

At this point it is worthwhile to compare the physical properties of $Nd_{1-x}Pb_xMnO_3$ with other manganites. It may be emphasized here that, the ground state of mixed valent manganites for a given divalent dopant concentration (x) is mainly dependent on average cationic radius ($\langle r_A \rangle$) [18]. A larger $\langle r_A \rangle$ enhances the bandwidth of e_g electrons of the Mn ions. This stabilizes the ferromagnetic metallic (FM) phase at low temperature favoring double exchange (DE) interaction. Lower values of $\langle r_A \rangle$ result in narrow e_g electron bandwidth. In this case, the kinetic energy of itinerant e_g electrons is not high enough to enable a charge delocalization. Hence, these systems may achieve a charge-ordered (CO) antiferromagnetic (AFM) ground state which is electrically insulating or a ferromagnetic insulating ground state. The transition from an insulating to metallic phase occurs with the increase of effective cationic radius by substitution of rare earth site (R-site) cation with any divalent ion. For example, the MI transition sets-in for $Nd_{1-x}Pb_xMnO_3$ at $x = 0.2$. However, it happens at $x = 0.25$ for $La_{1-x}Ca_xMnO_3$ and at $x = 0.18$ for $La_{1-x}Sr_xMnO_3$ as reported in the phase diagrams. On the other hand, $Pr_{1-x}Ca_xMnO_3$ has no MI transition because of low value of $\langle r_A \rangle$ [29]. Interestingly, the phase diagram for $Nd_{1-x}Pb_xMnO_3$ [30] is different from that of $Nd_{1-x}Sr_xMnO_3$ [9], although ionic radii of Pb^{2+} and Sr^{2+} are similar. Furthermore, the change of structure as a function of divalent dopant concentration for $Nd_{1-x}Pb_xMnO_3$ is quite different from those for other manganites as described earlier. The influence of Nd moments on magnetization or AC susceptibility is unique property in $Nd_{1-x}Pb_xMnO_3$. This is not present in other rare earth manganites ($La_{1-x}Ca_xMnO_3$ or $La_{1-x}Sr_xMnO_3$).

Table 5
Mn–Mn distances and corresponding interactions in pure ($x = 0$) (Ref. [24]) and doped $NdMnO_3$ structures

Formula	Mn–Mn distance (Å)	Interaction
$NdMnO_3$	3.7945(6)	AFM (out of plane)
	3.9342(4)	FM (in plane)
$Nd_{0.75}Pb_{0.25}MnO_{2.72}$	3.8836, 3.8878, 3.876	FM (DE)
$Nd_{0.62}Pb_{0.38}MnO_{2.7}$	3.8654, 3.8674	FM (DE)

6. Conclusions

The structure of $Nd_{1-x}Pb_xMnO_3$ single crystals is determined for $x = 0.25$. The structural study extended to higher dopant concentrations reveals that the structure is cubic at $x = 0.38$. Structural changes from orthorhombic → tetragonal → cubic are discernible with increasing dopant concentration (x). No evidence for twinning is observed in electron diffraction experiments. The MnO_6 octahedral distortion and inter octahedral tilt are removed progressively with higher doping. A correlation between the modulation in structure and physical properties has been presented. It is observed that, insulator to metal as well as paramagnetic to ferromagnetic transition temperatures are sensitive to divalent doping concentration.

Acknowledgements

This work is supported by CSIR through an extramural research grant which is gratefully acknowledged. We thank the Department of Science and Technology, India for data collection on the CCD facility setup under the IRPHA-DST program.

References

[1] M.A. Gilleo, Acta Crystallogr. 10 (1957) 161.
[2] W.C. Yi, S.I. Kwun, J.G. Yoon, J. Phys. Soc. Jpn. 69 (2000) 2706.
[3] E. Pollert, S. Krupicka, E. Kuzmicova, J. Phys. Chem. Solids 43 (1982) 1137.
[4] P.G. Radaelli, M. Marezio, H.Y. Hwang, S.W. Cheong, J. Solid State Chem. 122 (1996) 444.
[5] D.N. Argyriou, D.G. Hinks, J.F. Mitchell, C.D. Potter, A.J. Schultz, D.M. Young, J.D. Jorgensen, S.D. Bader, J. Solid State Chem. 124 (1996) 381.
[6] J.F. Mitchell, D.N. Argyriou, C.D. Potter, D.G. Hinks, J.D. Jorgensen, S.D. Bader, Phys. Rev. B 54 (1996) 6172.
[7] J. Topfer, J.B. Goodenough, J. Solid State Chem. 130 (1997) 117.
[8] A. Urushibara, Y. Moritomo, T. Arima, A. Asamitsu, G. Kido, Y. Tokura, Phys. Rev. B 51 (1995) 14103.
[9] R. Kajimoto, H. Yoshizawa, H. Kawano, H. Kuwahara, Y. Tokura, K. Ohoyama, M. Ohashi, Phys. Rev. B 60 (1999) 9506.
[10] N.W. Thomas, Acta Crystallogr. B 54 (1998) 585.
[11] C.N.R. Rao, A.K. Raychaudhuri, in: C.N.R. Rao, B. Raveau (Eds.), Colossal Magnetoresistance, Charge Ordering and Related Properties of Manganese Oxides, World Scientific, Singapore, 1998, p. 3.
[12] J.F. Mitchell, D.N. Argyriou, J.D. Jorgensen, in: Y. Tokura (Ed.), Colossal Magnetoresistive Oxides, Gordon & Breach Science Publishers, New York, 2000, p. 189.
[13] H.L. Ju, J. Gopalakrishnan, J.L. Peng, Qi Li, G.C. Xiong, T. Venkatesan, R.L. Greene, Phys. Rev. B 51 (1995) 6143.

[14] C. Mitra, P. Raychaudhuri, K. Dorr, K.H. Mueller, L. Schultz, P.M. Oppeneer, S. Wirth, Phys. Rev. Lett. 90 (2003) 17202.
[15] J.B. Torrance, P. Lacorre, A.I. Nazzal, E.J. Ansaldo, Ch. Niedermayer, Phys. Rev. B 45 (1992) 8209.
[16] J.B. Goodenough, in: J.B. Goodenough (Ed.), Structure and Bonding, vol. 98, Springer, Berlin, Heidelberg, 2001, p. 7.
[17] J. Kanamori, J. Phys. Chem. Solids 10 (1959) 87.
[18] J.M.D. Coey, M. Viret, S. von Molnar, Adv. Phys. 48 (1999) 167.
[19] N. Ghosh, S. Elizabeth, H.L. Bhat, G.N. Subanna, M. Sahana, J. Magn. Magn. Mater. 256 (2003) 286.
[20] Bruker, SMART and SAINT, Bruker AXS Inc., 1998, Madison, Wisconsin, USA.
[21] G.M. Sheldrick, SHELXL-97, 1997, University of Gottingen, Germany.
[22] K.S. Aleksandrov, Ferroelectrics 14 (1976) 801.
[23] H. Barnighausen, Acta Crystallogr. A 31 (1975) S31.
[24] A. Munoz, J.A. Alonso, M.J. Martinez-Lope, J.L. Garcia Munoz, M.T. Fernandez-Diaz, J. Phys.: Condens. Matter 12 (2000) 1361.
[25] H.Y. Hwang, S.W. Cheong, P.G. Radaelli, M. Marezio, B. Batlogg, Phys. Rev. Lett. 75 (1995) 914.
[26] P.G. Radaelli, M. Marezio, H.Y. Hwang, S.W. Cheong, B. Batlogg, Phys. Rev. B 54 (1996) 8992.
[27] J.B. Goodenough, Phys. Rev. 100 (1955) 564.
[28] P.W. Anderson, H. Hesegawa, Phys. Rev. 100 (1955) 675.
[29] Y. Tokura, in: Y. Tokura (Ed.), Colossal Magnetoresistive Oxides, Gordon & Breach Science Publishers, New York, 2000, pp. 1–52.
[30] N. Ghosh, S. Elizabeth, H.L. Bhat, P.L. Paulose, J. Appl. Phys., 96 (2004) 3346.